Applied Physics A (2019) 125:788
https://doi.org/10.1007/s00339-019-3094-7

Applied Physics A
Materials Science & Processing

Preparation of WO_3/g-C_3N_4 composites with enhanced photocatalytic hydrogen production performance

Peng Xing[1] · Feng Zhou[1] · Zhelun Li[1]

Received: 8 August 2019 / Accepted: 22 October 2019 / Published online: 29 October 2019

Abstract
Tungsten trioxide was prepared by a hydrothermal method, and WO_3/g-C_3N_4 composite photocatalysts were prepared in two steps by hydrothermal synthesis and muffle furnace calcination. The hydrogen production experiment was carried out using g-C_3N_4 and WO_3/g-C_3N_4 composites under simulated visible light irradiation. The samples were characterized by X-ray diffraction (XRD), field emission scanning electron microscopy (SEM), ultraviolet–visible diffuse reflectance spectroscopy (DRS), Fourier transform infrared spectroscopy (FT-IR) and Brunauer–Emmett–Teller (BET) analysis. It was found that $WO_3(H_2O)_{0.333}$ prepared by hydrothermal treatment is nanorod-like and forms an effective combination with lamellar g-C_3N_4. The hydrogen production rate of the optimal sample is 224.4 μmol/h, which is twice that of pure g-C_3N_4. The addition of tungsten trioxide improves the separation efficiency of photogenerated electron–hole pairs and contributes to the improvement in the photocatalytic performance. This is of great significance to the application of modified g-C_3N_4.

1 Introduction

More and more researches have been devoted to the clean and renewable method of photocatalytic hydrogen production since it was discovered by Honda and Fujishima [1]. A variety of catalysts, including high molecular polymers, metal oxides, and sulfides, are synthesized to find more efficient and more active photocatalysts by coupling, introduction of defects, and deposition of precious metals [2–7].

Conventional catalysts such as TiO_2 absorb sunlight mainly in the ultraviolet region, which is a small part of sunlight [8, 9]. In 2009, Wang et al. developed a nonmetallic covalent compound defined as g-C_3N_4. He realized the visible light decomposition of hydrogen and explained the mechanism of its photocatalysis [10]. In addition to its visible light response, g-C_3N_4 could obtain a larger specific surface area after specific treatment [11]. However, the photogenerated electron–hole pairs can exist for a short period of time and quickly recombine. And there are few active sites and low activity of g-C_3N_4 [12–14]. To overcome these short boards, a lot of researches have been invested. Jiang et al. doped g-C_3N_4 nanosheets with phosphorus and introduced carbon defects to increase its light absorption, which greatly improved the photocatalytic hydrogen production rate [15]. Jing et al. reported mineral acid or phosphoric acid etching of g-C_3N_4 nanosheets to increase the number of active sites, which greatly improved the photocatalytic hydrogen production rate [16]. On the other hand, to reduce the recombination of photogenerated electron and hole pairs, heterojunction composite photocatalysts have been widely synthesized [17–20].

WO_3 has a large forbidden bandwidth and can be designed to form a heterojunction with other materials. There are some reports with different treatments on WO_3/g-C_3N_4 heterojunction photocatalysts [21, 22]. Yu et al. prepared an ultrathin two-dimensional WO_3/ g-C_3N_4 composite heterojunction photocatalyst. This Z-scheme system effectively improved the photocatalytic activity of pure g-C_3N_4 [23]. Tahir et al. prepared a WO_3/g-C_3N_4 composite photocatalyst. The main reason for the increased photocatalytic hydrogen production activities was that it has extended the light absorption [24]. In addition to its reducing hydrogen production, the WO_3/g-C_3N_4 composite photocatalyst can also be used to degrade the organic pollutants such as ciprofloxacin, fuchsin and tetracycline [21, 25, 26].

In this paper, WO_3 was prepared by a hydrothermal method, and a WO_3/g-C_3N_4 composite was synthesis by mixing WO_3 and melamine as precursors. To find the

✉ Feng Zhou
zhoufeng@dlmu.edu.cn

[1] Key Laboratory of Ship-Machinery Maintenance and Manufacture for Ministry of Transport, Dalian Maritime University, Dalian 116026, People's Republic of China

optimal ratio by changing the amount of WO_3 addition, the mechanism of photocatalytic performance improvement of the WO_3/g-C_3N_4 composites is analyzed and discussed.

2 Experimental

2.1 Materials

All analytical grade chemicals, melamine, methanol, sodium tungstate (Na_2WO_4•H_2O), and chloroplatinic acid (H_2PtCl_6•$6H_2O$) were used without further purification.

2.2 *Synthesis of WO_3 nanorods*

First, 1 g of Na_2WO_4·H_2O was weighed and sonicated in 70 ml of deionized water for 30 min until fully dissolved. After diluting concentrated hydrochloric acid to 4 mol/l, it was added dropwise to the aqueous solution of sodium tungstate to adjust the pH to 1. The solution was transferred to a polytetrafluoroethylene reaction vessel, heated to 180℃, incubated for 24 h and then cooled to room temperature with the furnace. Finally, the obtained sample was washed several times with deionized water and absolute ethanol and dried at 60 ℃ for 12 h.

2.3 Synthesis of WO_3/g-C_3N_4 nanoarchitecture

Fifteen milligrams of tungsten trioxide was weighed and added to 20 ml of alcohol, and 2.4 g of melamine was weighed, added to the above solution for 1 h and then magnetically stirred for 3 h. After the above solution was placed in an oven and dried at 60 ℃, the obtained solid was placed in a crucible, heated to 550 ℃ in a muffle furnace at a rate of 10 ℃/min and allowed to cool to room temperature after 3 h of incubation. According to the amount of tungsten trioxide added to the melamine, the obtained composite samples were labeled as WG*x*, where *x* represents *x* mg tungsten trioxide added.

2.4 Characterization

X-ray diffraction (XRD) patterns were characterized with a Rigaku-DMAX Ultima$^+$ diffractometer equipped with cobalt target. The scan range was from 10° to 90°, respectively. The microscopic morphology was observed using scanning electron microscopy (SEM) (SUPRA 55 SAPPHIRE). Optical properties were analyzed using an ultraviolet–visible spectrophotometer (DRS, TU-1901), respectively. The functional group of the composite samples and the bond between WO_3 and g-C_3N_4 were analyzed using a FT-IR spectrometry (PerkinElmer Frontier spectrometer). The specific surface area test (BET) was analyzed with a WBL-810-type specific surface area and void fraction analyzer.

3 Results and discussion

3.1 Structure characterization

The XRD data of g-C_3N_4, WO_3 and composite samples are shown in Fig. 1. For WO_3, the diffraction peaks correspond to (0 2 0) (0 0 2) (2 2 0) (2 2 2) and (2 2 2 4) facets at 16.40°, 26.74°, 32.79°, 42.80° and 65.61°, respectively, and their lattice spacing can be attributed to 0.63 nm, 0.39 nm, 0.32 nm, 0.25 nm and 0.17 nm. The diffraction peak corresponds to (0 0 2) facet of g-C_3N_4 at 31.83°, while the diffraction peak corresponds to the (1 0 0) facet at 14.94°, respectively. The hydrothermally prepared WO_3, which is $WO_3(H_2O)_{0.333}$, is provided with water of crystallization corresponding to PDF card 87–1203, and the WO_3 powder is dehydrated when it is calcined with melamine. In the composite sample from which the crystallization water was removed, the phase of WO_3 still appeared. The disappearance of (1 1 1) crystal face at 21.023° was probably due to the removal of the water of crystallization. Meanwhile, since the characteristic peak of g-C_3N_4 is at 14.94° and 31.83°, the composite sample has a superposition of the characteristic peaks at these two places, and with the increase in WO_3, the superposition effect of g-C_3N_4 is gradually weakened, and the characteristic peak of WO_3 gradually increases.

The functional group of the composite samples and the bond between WO_3 and g-C_3N_4 were detected with the Fourier transform infrared spectroscopy. As shown in Fig. 2, the peaks of the composite samples are similar to those of g-C_3N_4 and the peaks at 1238, 1316, 1461 and 1640 cm^{-1}

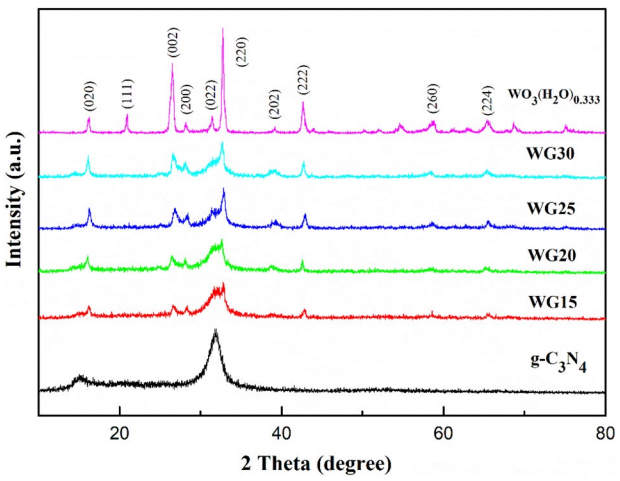

Fig. 1 XRD patterns for g-C_3N_4 and WO_3 nanosheets and their composites

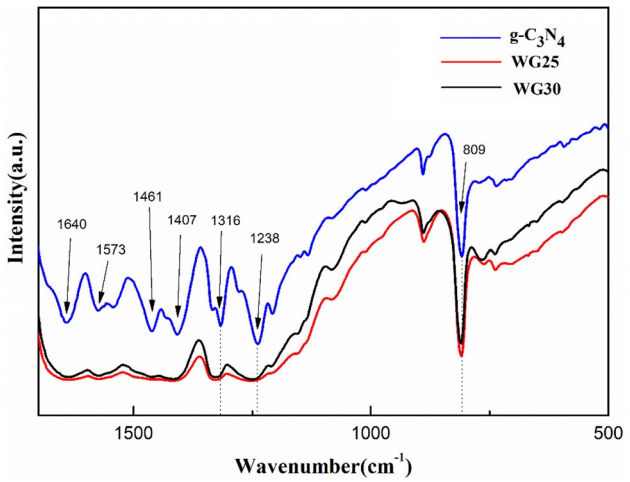

Fig. 2 FT-IR spectra of g-C_3N_4, WG25 and WG30

can be attributed to C–N. The peak at 809 cm^{-1} is related to s-triazine [27, 28]. However, the composite samples showed a shift at the 1238, 1316, and 809 cm^{-1} positions. The blueshift at 1238 and 1316 cm^{-1} was due to the N atom in the g-C_3N_4 bonding with the more electronegative O atom in WO_3, and the force constant increased so that the absorption moved toward the high wavenumber direction. Because s-triazine produces a conjugation effect, the bond length becomes shorter and the peak shifts toward a higher wavenumber, so another blueshift occurs at 809 cm^{-1}. The shift in the functional groups demonstrates the formation of chemical bonds between tungsten trioxide and g-C_3N_4 in the composite.

Figure 3 displays the ultraviolet–visible diffuse reflectance spectroscopy of pure g-C_3N_4 and the WO_3/g-C_3N_4 composites. It can be observed in Fig. 3a that the absorption of visible light by the composite samples significantly improved after the addition of tungsten trioxide. More importantly, as can be seen in Fig. 3b, the forbidden band width of the composite samples did not greatly increase with the addition of tungsten trioxide and remained similar to that of g-C_3N_4, which could increase the partial absorption of visible light.

The forbidden band width can be calculated by the following empirical formula [29]:

$$E_g = 1240/\lambda_g, \tag{1}$$

where λ_g is the maximum absorption edge of the sample. According to this equation, the bandgap energies of g-C_3N_4, WO_3, WG15, WG20, WG25 and WG30 are 2.74 eV, 3.19 eV, 2.74 eV, 2.75 eV, 2.79 eV, and 2.80 eV, respectively. The valence band potential and conduction band potential of the WO_3/g-C_3N_4 composite samples can be calculated by the following equations [30, 31]:

$$E_{VB} = X - E_X + 0.5E_g, \tag{2}$$

$$E_{CB} = E_{VB} - E_g, \tag{3}$$

where X is the electronegativity of the semiconductor, $X = (X(A)^a X(B)^b)^{1/(a+b)}$ [32]. The X value for WO_3 is 6.59 eV. E_X is the reduction potential of water (4.5 eV). The sample bandgap, valence band potential and conduction band potential obtained by calculation are shown in Table 1. The E_g of g-C_3N_4 and WO_3 was assumed to be 2.74 eV and 3.19 eV. The E_{CB} of WO_3 and g-C_3N_4 was assumed to be 0.49 eV and − 1.14 eV. The E_{VB} of WO_3 and g-C_3N_4 was determined to be 3.68 eV and 1.60 eV.

Table 1 The bandgap, VB and CB of WO_3 and g-C_3N_4

Sample	Bandgap (eV)	VB (eV)	CB (eV)
WO_3	3.19	3.68	0.49
g-C_3N_4	2.74	1.60	− 1.14

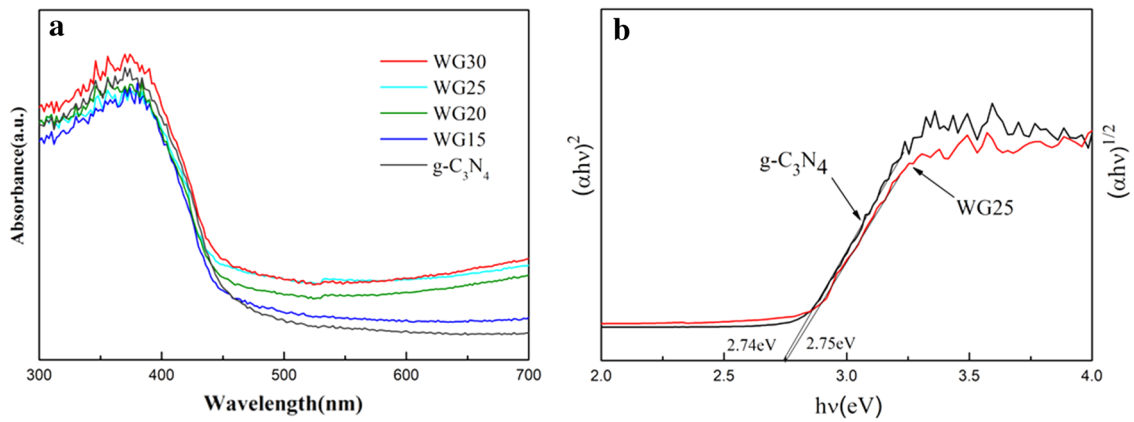

Fig. 3 **a** UV–Vis spectra of g-C_3N_4 and the WO_3/g-C_3N_4 composites and **b** corresponding bandgap information for g-C_3N_4 and WG25

The Brunauer–Emmett–Teller (BET) analysis of g-C_3N_4 and the composites were detected with nitrogen adsorption–desorption analysis. Figure 4 shows the adsorption–desorption isotherm curves of g-C_3N_4 and WO_3 and their pore size distribution. The specific surface areas of the composite samples are similar. The pore volume distribution of WG25 is 0.0008 cm^3/g, which is approximately twice the pore volume of pure g-C_3N_4, and a larger pore volume can provide more reactive sites for the production of hydrogen.

3.2 Morphological characteristics

SEM can observe the morphology of a material from the microscopic view and judge the size of a material. Figure 5a–c shows the SEM images of g-C_3N_4, pure tungsten trioxide nanorods and the composite samples, respectively. As shown in Figure 5a–c, g-C_3N_4 is in the form of a sheet, the tungsten trioxide is in the form of rods, and the WO_3 nanorods are inserted in the g-C_3N_4 layer. A tight junction is appeared at the interface between WO_3 and g-C_3N_4. This effective contact surface shortens the moving distance of the photogenerated electrons and ensures the transmission efficiency of electrons between the interfaces, which is more conducive to the transfer of electrons. The results of EDS mapping are shown in Fig. 6a–e. The existence of C, N, O, W and their distribution characteristics can be clearly observed. The WO_3 nanorods were inserted into the g-C_3N_4 nanosheets. All the elements were evenly distributed.

As shown in Fig. 7a, g-C_3N_4 has a two-dimensional sheet distribution with wrinkles. Figure 7b is a TEM image of WO_3, and the rod structure of WO_3 can be more clearly seen in the figure. Figure 7d is a partial enlarged view of Fig. 7c, and it is apparent that WO_3 nanorods are well attached to the surface of g-C_3N_4 layer. The lattice spacings inside WO_3 are 0.387 nm and 0.31 nm, which can be attributed to the (0 0 2) and (0 4 0) planes, respectively. The data are consistent with previous reports. The g-C_3N_4 nanosheets have no

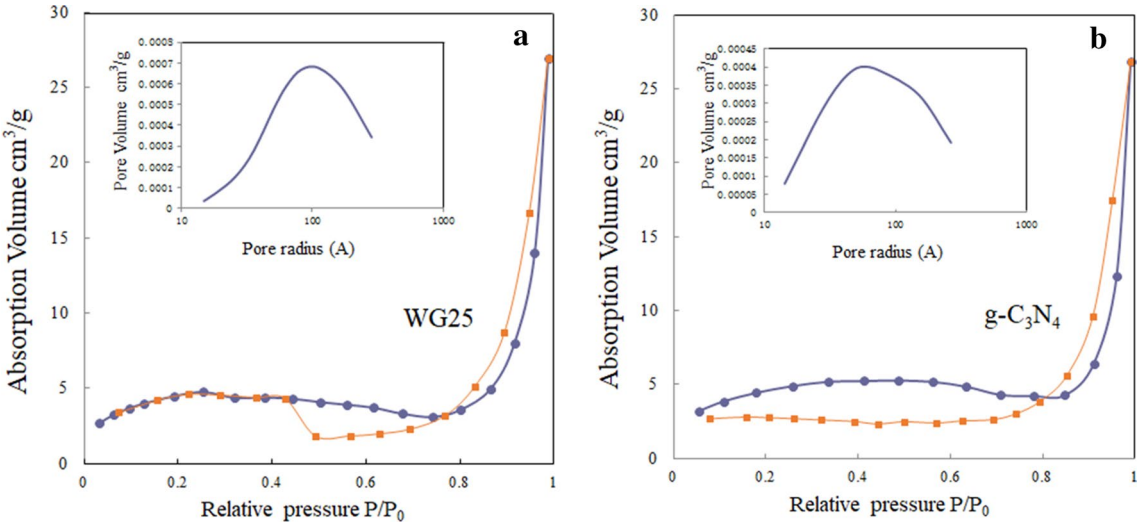

Fig. 4 Nitrogen adsorption–desorption isotherm curves of the composite: **a** WG25 and **b** g-C_3N_4. The insets show the BJH pore-radius distribution of WO_3 and g-C_3N_4

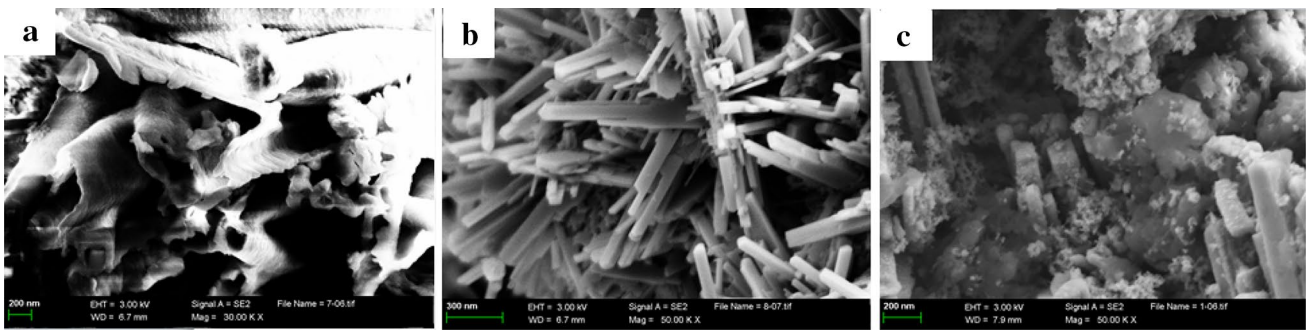

Fig. 5 SEM images of g-C_3N_4 (**a**), WO_3 nanorods (**b**) and WO_3/g-C_3N_4 composite samples (**c**)

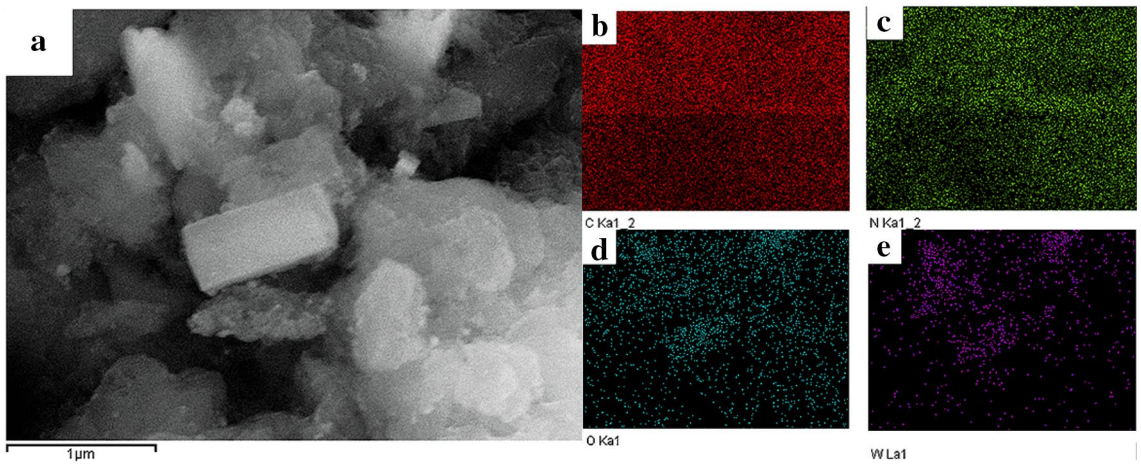

Fig. 6 Elemental mapping of **a** WG30 and **b–e** the corresponding elemental mapping images of C, N, O and W

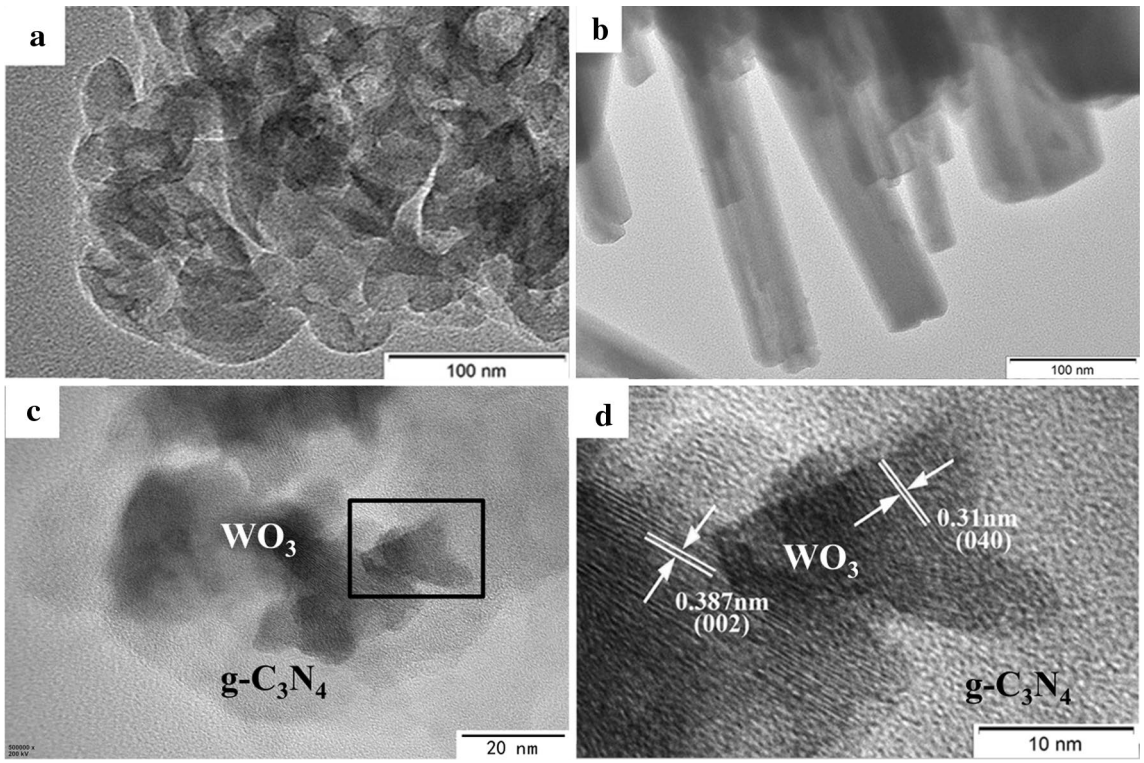

Fig. 7 TEM images of g-C_3N_4 (**a**) and WO_3 (**b**) and HRTEM images of WG30 (**c**, **d**)

obvious crystal lattice, which is due to the poor crystallinity of g-C_3N_4 and is consistent with the existing literature reports.

3.3 Photocatalytic activity

To detect the rate of hydrogen production, a xenon lamp was used to simulate sunlight, methanol was used as a sacrificial agent and chloroplatinic acid as a promoter. The amount of hydrogen produced was measured every half an hour. As shown in Fig. 8, pure WO_3 did not detect significant hydrogen production because its conduction band position was more positive than H^+ of water. Pure g-C_3N_4 had obvious hydrogen production activity. With the addition of WO_3, the hydrogen production of the composites was greatly improved. In particular, the optimal sample WG25

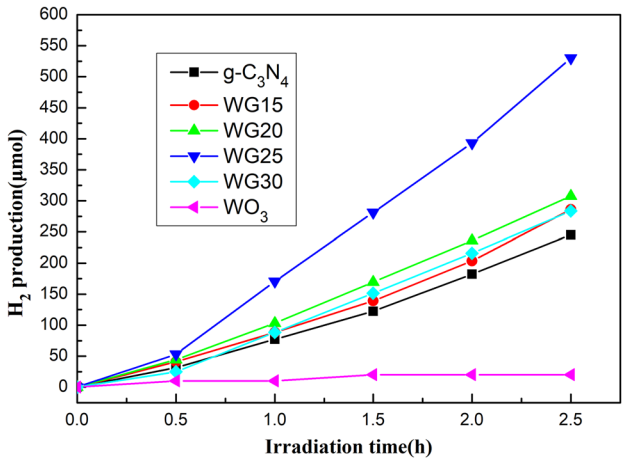

Fig. 8 Comparison of the H2-generation activities of the as-prepared samples under xenon lamp irradiation

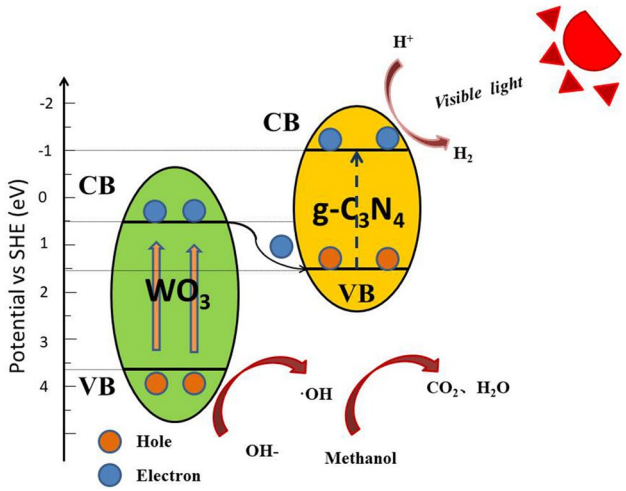

Fig. 9 Z-scheme mechanism over WO_3/g-C_3N_4

had the highest hydrogen production rate of 224.4 μmol/h, its activity was approximately twice as high as that of the pure g-C_3N_4 nanosheets. With the further increase of WO_3, the hydrogen production rate of the composite samples was rather reduced, because too much WO_3 reduced its light response.

3.4 Mechanism discussion

Figure 9 shows the photocatalytic mechanism. When sunlight is irradiated onto g-C_3N_4, the electrons on the valence band of the g-C_3N_4 nanosheets are excited and transferred to the conduction band. The E_{CB} of WO_3 and the E_{VB} of g-C_3N_4 were determined to be 0.49 eV and 1.60 eV. Since the conduction band of WO_3 is close to the valence band of g-C_3N_4, the electrons photogenerated by WO_3 are easily combined with the holes of g-C_3N_4 during the transfer process. Meanwhile, the holes of WO_3 are captured by hydroxide to generate hydroxyl radicals, and the hydroxyl radicals are transferred to the surface of the catalyst to oxidize methanol into water and CO_2. The photogenerated electrons transferred to the g-C_3N_4 conduction band reduce H^+ to hydrogen. When a Z-scheme heterojunction is formed by adding g-C_3N_4 to WO_3, its oxidative and reductive properties are both improved [33].

4 Conclusions

In summary, WO_3 was prepared by a hydrothermal method, and a WO_3/g-C_3N_4 composite was synthesized by hydrothermal synthesis and muffle furnace calcination using Na_2WO_4•H_2O and melamine as precursors. The addition of WO_3 significantly increased the hydrogen production rate of the composite sample, and the optimal activity of WG25 reached 224.4 μmol/h. With the further increase of WO_3, the hydrogen production rate of the composite sample was rather reduced, because too much WO_3 reduced its light response. XRD, EDS, FT-IR and TEM results further confirmed the presence of a Z-scheme heterojunction mechanism. This is of great significance to the application of modified g-C_3N_4.

Acknowledgements This work is supported by the National Natural Science Foundation of China (nos. 51879018, 51771042 and 21676040) and the Fundamental Research Funds for the Central Universities (nos. 3132016065 and 3132016341).

References

1. A. Fujishima, K. Honda, Nature **238**, 37–38 (1972)
2. S.A.A. Terohid, S. Heidari, A. Jafari, S. Asgary, Appl. Phys. A. **124**, 567 (2018)
3. F. Zhang, H.Q. Zhuang, W.M. Zhang, J. Yin, F.H. Cao, Y.X. Pan, Catal. Today. **330**, 203–208 (2019)
4. S.W. Cao, J.G. Yu, J. Photochem. Photobiol. C. **27**, 72–99 (2016)
5. Q.H. Shen, R.H.N. Bi, L.F. Wei, D.D. Hao, N.X. Li, J.C. Zhou, Int. J. Hydrog. Energy **44**, 14550–14560 (2019)
6. X.J. Zhou, H. Yu, D. Zhao, X.C. Wang, S.T. Zheng, Appl. Catal. B Environ. **248**, 423–429 (2019)
7. J.H. Qiu, X.G. Zhang, Y. Feng, X.F. Zhang, H.T. Wang, J.F. Yao, Appl. Catal. B Environ. **231**, 317–342 (2018)
8. L.X. Sang, H. Ge, B.W. Sun, Int. J. Hydrog. Energy **44**, 15787–15794 (2019)
9. C.A. Roberts, S.P. Phivilay, I.E. Wachs, Chin. Chem. Lett. **29**, 769–772 (2018)
10. X. Wang, K. Maeda, A. Thomas, K. Takanabe, G. Xin, J.M. Carlsson, K. Domen, M. Antonietti, Nat. Mater. **8**, 76–80 (2009)
11. Y.J. Yuan, Z.K. Shen, S.T. Wu, Y.B. Su, L. Pei, Z.G. Ji, M.Y. Ding, W.F. Bai, Y.F. Chen, Z.T. Yu, Z.G. Zou, Appl. Catal. B Environ. **246**, 120–128 (2019)
12. Q.C. He, F. Zhou, S. Zhan, N.B. Huang, Y. Tian, Appl. Surf. Sci. **430**, 325–334 (2018)

13. L. Liang, L. Shi, F.X. Wang, L.Z. Yao, Y. Zhang, W. Qi, J. Hydrog. Energy **44**, 16315–16326 (2019)
14. J.Y. Tang, W.G. Zhou, R.T. Guo, C.Y. Huang, W.G. Pan, P.C. Liu, Energy Proc. **158**, 1553–1558 (2019)
15. S.E. Guo, Y.Q. Tang, Y. Xie, C.G. Tian, Q.M. Feng, W. Zhou, B.J. Jiang, Appl. Catal. B Environ. **218**, 664–671 (2017)
16. Z.J. Li, F. Raziq, C. Liu, L.L. Bai, L.Q. Jing, Curr. Opin. Environ. Sustain. **6**, 57–62 (2017)
17. L. Chen, Y.M. Xu, B.L. Chen, Appl. Catal. B Environ. **256**, 117848 (2019)
18. Y. Li, K. Lv, W. Ho, F. Dong, X. Wu, Y. Xia, Appl. Catal. B Environ. **202**, 611–619 (2017)
19. X.B. Qian, W. Peng, J.H. Huang, Mater. Res. Bull. **102**, 362–368 (2018)
20. S.L. Deng, Z.B. Yang, G.J. Lv, Y.Q. Zhu, H.C. Li, F.M. Wang, X.B. Zhang, Appl. Phys. A. **44**, 125 (2019)
21. J.Y. Chen, X.Y. Xiao, Y. Wang, Z.H. Ye, J. Appl. Surf. Sci. **467–468**, 1000–1010 (2019)
22. X. Liu, A.L. Jin, Y.S. Jia, T.L. Xia, C.X. Deng, M.H. Zhu, C.F. Chen, X.S. Chen, Appl. Surf. Sci. **405**, 359–371 (2017)
23. J.W. Fu, Q.L. Xu, J.X. Low, C.J. Jiang, J.G. Yu, Appl. Catal. B Environ. **243**, 556–565 (2019)
24. M.B. Tahir, M. Rafique, M. Isa Khan, A. Majid, F. Nazar, M. Sagir, S. Gilani, M. Farooq, A. Ahmed, Int. J. Energy Res. **42**, 4667–4673 (2018)
25. L. Na, P. Wang, S. Yan, H.T. Yu, N. Liu, Q. Xie, Chemosphere **215**, 444–453 (2019)
26. S.F. Chen, Y.F. Hu, S.G. Meng, X.L. Fu, Appl. Catal. B Environ. **150–151**, 564–573 (2014)
27. Y. Tian, F. Zhou, S. Zhan, Z.Y. Zhu, Q.C. He, J. Photochem. Photobiol. A. **350**, 10–16 (2018)
28. S. Zhan, F. Zhou, N.B. Huang, Y.F. Yin, M. Wang, Y.F. Yang, Y.J. Liu, J. Mol. Catal. A Chem. **401**, 41–47 (2015)
29. Y.P. Zhang, X.Q. Hao, X.L. Ma, H. Liu, Z.L. Jin, Int. J. Hydrog. Energy **44**, 13232–13241 (2019)
30. S. Zhan, F. Zhou, N.B. Huang, Y.F. Yang, Y.J. Liu, Y.F. Yin, Y.N. Fang, Appl. Surf. Sci. **358**, 328–335 (2015)
31. Y.Z. Li, F. Zhou, Z.Y. Zhu, F. Wu, Appl. Surf. Sci. **467–468**, 819–824 (2019)
32. J. Jin, J.G. Yu, D.P. Guo, C. Cui, W.K. Ho, Small. **11**, 5262–5271 (2015)
33. G.C. Chen, S.C. Bian, C.Y. Guo, X.R. Wu, Mater. Lett. **23**, 596–599 (2019)